Semnan University

Progress in Physics of Applied Materials

journal homepage: https://ppam.semnan.ac.ir/

Effect of Ba^{2+} Doping on the Crystal Structure and Optical Band Gap of $NdFeO_3$ Orthoferrite

Mansoureh Pourjafar, Davoud Sanavi Khoshnoud*

Faculty of Physics, Semnan University P. O. Box 35195-363, Semnan, Iran

ARTICLE INFO

Article history:
Received: 26 August 2025
Revised: 25 October 2025
Accepted: 11 November 2025
Published online: 3 December 2025

Keywords:
$NdFeO_3$;
Sol-gel method;
Crystal structure;
Optical band gap.

ABSTRACT

In this study, neodymium was substituted by divalent barium ion (Ba^{2+}) at various concentrations (x = 0, 0.1, 0.2, 0.3, and 0.4) in the neodymium orthoferrite structure, forming the composition $Nd_{1-x}Ba_xFeO_3$ via the sol–gel method. To evaluate the effects of Ba^{2+} substitution, detailed structural and optical characterizations were conducted at room temperature. The results indicated that, with increasing barium content, the unit cell volume, the average Fe–O–Fe bond length, and the tolerance factor exhibited an increasing trend. In contrast, the orthorhombic strain and the octahedral distortion angle of the FeO_6 decreased progressively with higher Ba^{2+} concentrations. These structural changes suggest a reduction in lattice distortion, indicating a gradual evolution of the crystal symmetry toward a higher-symmetry (tetragonal) phase. Furthermore, optical characterization revealed a significant reduction in the optical band gap, decreasing from 2.15 eV for the $NdFeO_3$ sample to 1.28 eV for the sample with x = 0.4. This reduction can be attributed to modifications in the electronic structure and the enhancement of optical properties induced by Ba^{2+} substitution. These findings highlight the potential of Ba-doped $NdFeO_3$ for real world applications, including visible light photo-catalysis, gas and chemical sensors, optoelectronic devices, and photo-electrochemical systems.

1. Introduction

Perovskites represent a versatile class of materials that have attracted considerable research attention due to the strong coupling between the spin, charge, and lattice degrees of freedom, resulting in a variety of unique physical properties. These compounds typically conform to the general chemical formula ABO_3, in which A and B are cations with different ionic radii. Because of their exceptional functional characteristics, perovskites are considered ideal candidates for use in sensors, solar cells, and catalysts [1-6]. Among the perovskite structured materials, rare-earth orthoferrites ($RFeO_3$) are recognized as oxide semiconductors with an optical band gap in the range of approximately 2.0 eV. In this class of compounds, variations in the Fe–O bond length, an important parameter governing the band gap, are generally insignificant [7]. However, through substitution at either the R-site or the Fe-site, notable modifications in the band gap of these materials can be achieved [8]. Thus, rational and controlled band gap tuning not only enhances their functional performance but also opens new opportunities for the development of applications in energy, photocatalytic, and sensing technologies [9, 10]. In this context, neodymium orthoferrite ($NdFeO_3$) with orthorhombic crystal structure and *Pbnm* space group has garnered attention due to its distinctive structural and optical features. One of the key properties of $NdFeO_3$ is the direct influence of its crystal structure and symmetry on its optical characteristics and band gap [11]. Previous studies have shown that

* Corresponding author.
E-mail address: dskhoshnoud@semnan.ac.ir

Cite this article as:
Pourjafar, M. and Sanavi Khoshnoud, D., 2026. Effect of Ba^{2+} Doping on the Crystal Structure and Optical Band Gap of $NdFeO_3$ Orthoferrite. *Progress in Physics of Applied Materials*, *6*(2), pp.117-126. DOI: 10.22075/ppam.2025.38809.1168

substitution of rare-earth ions such as Ce^{3+} or Sm^{3+} at the Nd-site in $NdFeO_3$ causes only marginal variations in the optical band gap due to minimal changes in Fe–O bond length [12, 13]. On the other hand, the substitution of divalent alkaline-earth ions (Ca^{2+}, Mg^{2+} and Sr^{2+}) in similar orthoferrites has been reported to induce significant band-gap narrowing and enhanced defect formation, mainly attributed to the introduction of oxygen vacancies and lattice strain [14-17]. However, despite these advances, studies on the effect of Ba^{2+} substitution in $NdFeO_3$ remain scarce. Owing to its larger ionic radius (1.35 Å) compared to Nd^{3+} (0.98 Å) and distinct electronic configuration, Ba^{2+} incorporation is expected to induce more pronounced lattice distortions and defect chemistry, thereby influencing the structural and optical behavior differently from other divalent dopants. In this study, the Nd^{3+} site in $Nd_{1-x}Ba_xFeO_3$ is substituted by different concentrations of Ba^{2+} (x = 0.1, 0.2, 0.3, and 0.4), and the resulting changes in structural, microstructural, and optical properties are systematically investigated. The aim is to elucidate the correlation between Ba^{2+} incorporation, lattice strain, and optical band gap modulation, thereby addressing the existing research gap and contributing to a deeper understanding of structure property relationships in Ba-doped orthoferrites.

2. Materials and Methods

In this study, $Nd_{1-x}Ba_xFeO_3$ (x = 0, 0.1, 0.2, 0.3, and 0.4) nanoparticles were synthesized using the sol–gel method, in accordance with our previous work [18]. This technique enables the production of homogeneous, high-purity nanoparticles with precise control over particle size and dopant distribution. The resulting powders were annealed at 1000 °C for 2 hours to achieve the desired crystallinity and phase purity. To thoroughly investigate the properties of the compounds, a comprehensive set of characterization techniques was employed. The crystal structure and phase identification were examined using a Philips PW 1830 XRD instrument over the 2θ range of 20°–70° with a step size of 0.04° at room temperature. The collected data were analyzed using the FullProf software based on the Rietveld refinement method. The crystallite size and lattice strain were estimated using both the Debye–Scherrer equation and the Williamson–Hall (W–H) method. Field-emission scanning electron microscopy (FE-SEM), model TESCAN BRNO-Mira3 LMU and voltage of 10 kV was used to examine the surface morphology and to estimate the particle size distribution. To confirm the elemental composition and stoichiometric ratios of the samples, EDX was performed. In addition, the optical band gap energy of the samples was determined by analyzing the diffuse reflectance spectra (DRS, Agilent Cary/300/100) in the wavelength range of 200–1200 nm. The optical band gap (E_g) values were then calculated using the Tauc method based on the DRS data through the Kubelka–Munk (K-M) function, considering a direct electronic transition.

3. Results and Discussion

3.1. Structural analysis

X-ray diffraction (XRD) was employed as an effective technique to examine the crystal structure and identify the phases formed in the synthesized samples. Based on the phase analysis performed using X'pert software on the XRD patterns (Fig. 1(a)), a secondary $BaFe_2O_3$ phase was detected at $2\theta \approx 28.44°$ in the $Nd_{1-x}Ba_xFeO_3$ compositions with x = 0.3 and x = 0.4. The presence of this impurity phase was more pronounced in the x = 0.4 sample (Fig. 2). A similar phenomenon has been reported for the Ba substitution in $LaFeO_3$, where secondary phases emerge at Ba concentrations exceeding 10% [19]. As illustrated in Figure 1(b), with increasing concentration of the substituting ions, the main diffraction peak gradually shifted toward lower angles. This behavior is consistent with previously reported results for Ba^{2+} substitution in $LaFeO_3$ and $BiFeO_3$ [19, 20] and can be attributed to the larger ionic radius of Ba^{2+} ($r_{Ba^{2+}}$ = 1.35 Å) compared to Nd^{3+} ($r_{Nd^{3+}}$ = 0.98 Å), which results in an increase in the interplanar distances.

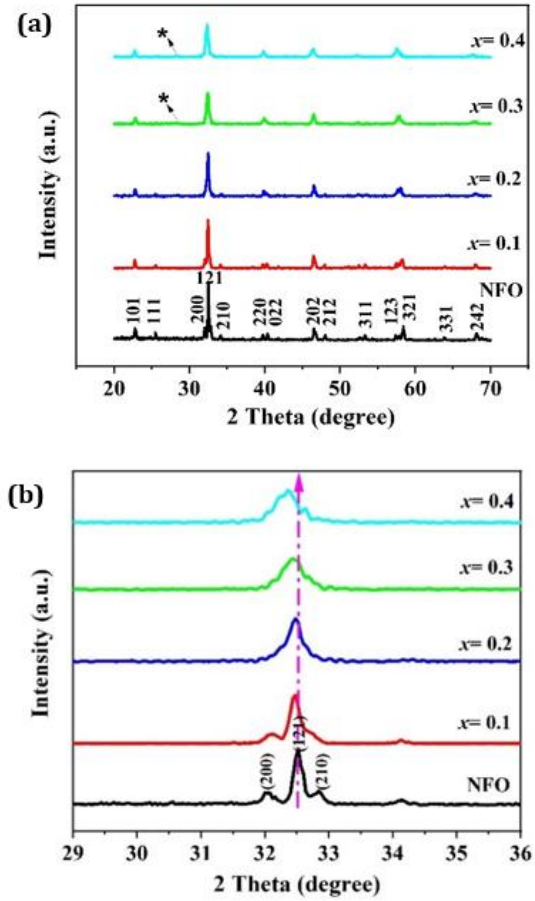

Fig. 1. (a) XRD pattern of the parent sample (NFO) and Ba-doped samples with different concentrations $Nd_{1-x}Ba_xFeO_3$ (* indicates the $BaFe_2O_3$ impurity phase) and **(b)** enlarged view of the main XRD peaks.

The refinement of X-ray patterns was carried out using the Rietveld method implemented in FullProf (Fig. 2), and the results are summarized in Table 1. The quality indicators obtained from the Rietveld refinement (R_p , R_{wp} and χ^2), reported in Table 1, confirm the reliability and accuracy of the structural model. As shown in Figure 3(a), the unit cell volume of the investigated samples increases with higher Ba^{2+} concentration. Since $r_{Nd^{3+}} < r_{Ba^{2+}}$, this increase in the unit cell volume is expected [19-21]. The variations in the lattice parameters with increasing Ba

content are presented in Figure 3(b). According to these results, parameters a and c increase with the Ba substitution, while parameter b decreases. The octahedral tilt angle (Φ) around the threefold [111] axis and the orthorhombic strain (S) were calculated using the following equations.

$$\Phi = cos^{-1}(\sqrt{2}\, a^2 / bc) \quad (1)$$

$$S = 2(b-a)/(b+a) \quad (2)$$

where a, b, and c are the lattice parameters [9, 22]. As depicted in Figure 3(c), the octahedral tilt angle (Φ) decreases with increasing Ba^{2+} concentration, whereas the orthorhombic strain (S) shows an increasing trend. The crystal structure stability was further assessed using the tolerance factor (τ), defined by Eq. 3:

$$\tau = \frac{(\mathrm{Nd/Ba-O})_{\mathrm{avg}}}{\sqrt{2}(\mathrm{Fe-O})_{\mathrm{avg}}} \quad (3)$$

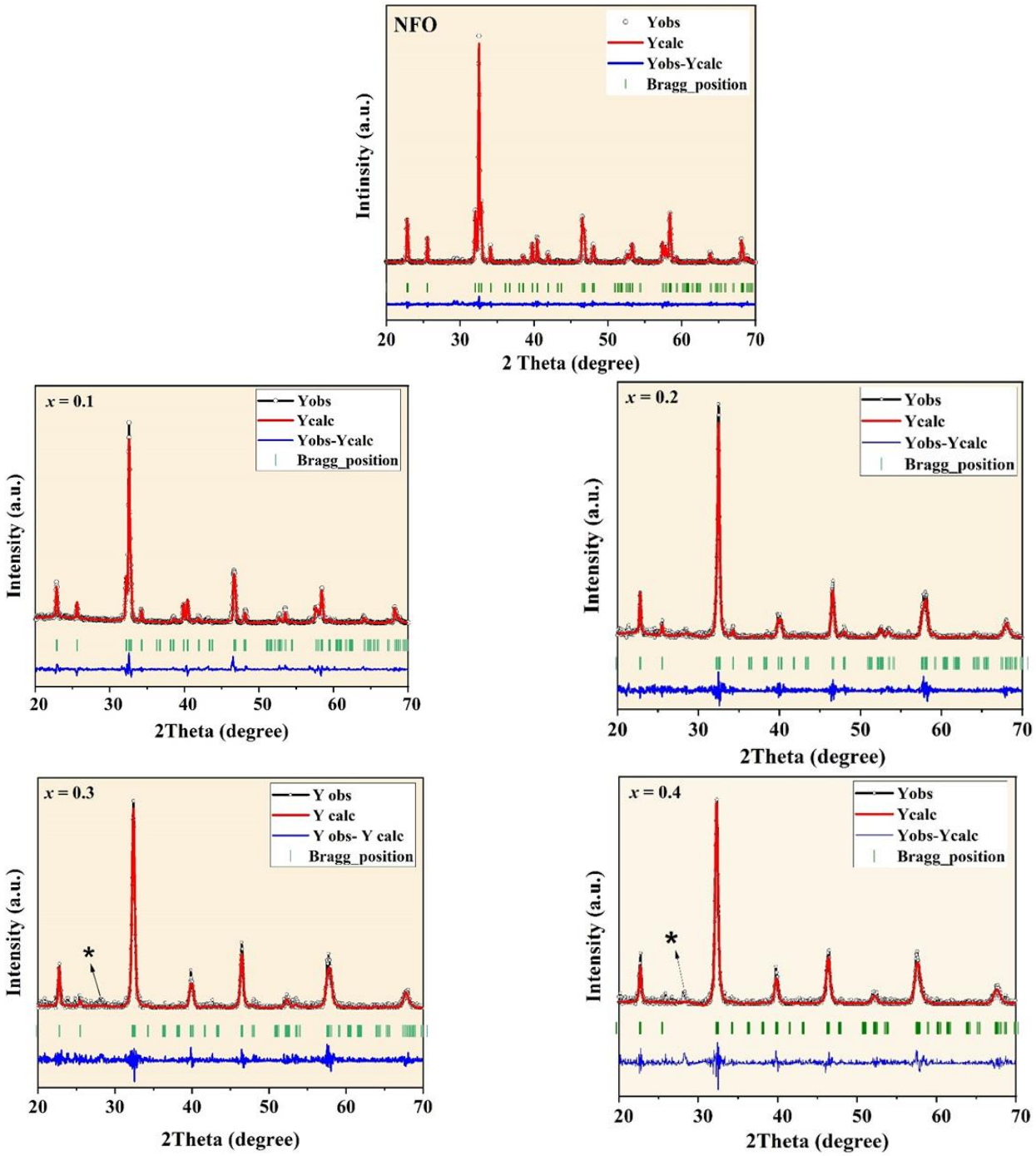

Fig. 2. Rietveld refinement of XRD pattern for $Nd_{1-x}Ba_xFeO_3$ samples with different Ba concentrations (* indicates the $BaFe_2O_3$ impurity phase).

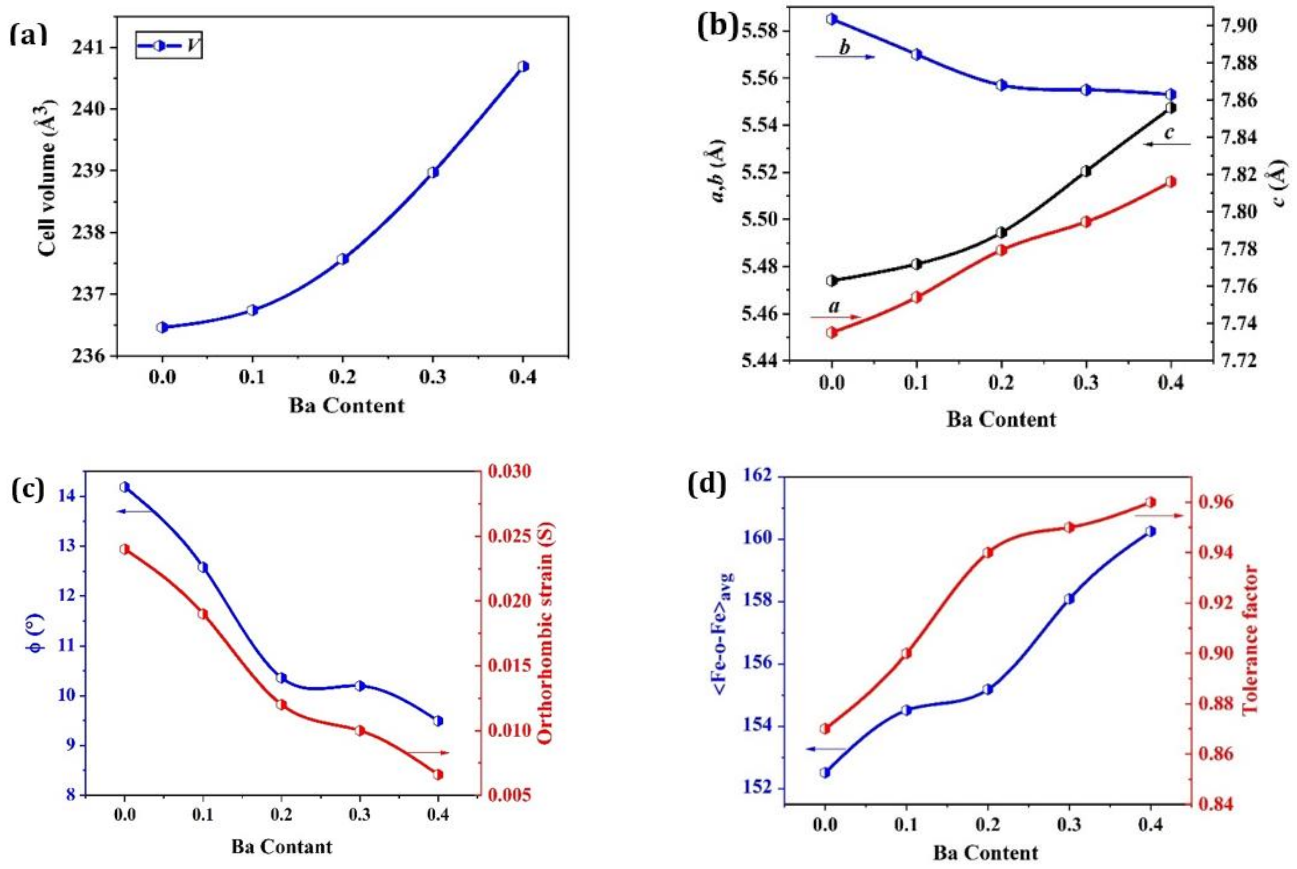

Fig. 3. Variations of **(a)** Unit cell volume ,**(b)** Lattice parameters (*a, b, c*) ,**(c)** Octahedral deviation angle of FeO_6 around the three-fold (111) axis and the orthorhombic strain, for $Nd_{1-x}Ba_xFeO_3$ samples, **(d)** Average Fe–O–Fe bond angle and the tolerance factor.

Table 1. Structural information along with quality indicators for the studied $Nd_{1-x}Ba_xFeO_3$ samples.

Sample	*NFO*	*x*=0.1	*x*=0.2	*x*=0.3	*x*=0.4
Space group	*Pbnm*	*Pbnm*	*Pbnm*	*Pbnm*	*Pbnm*
Lattice parameters					
a (Å)	5.452 (6)	5.467 (6)	5.487 (7)	5.499 (4)	5.516 (1)
b (Å)	5.585 (9)	5.570 (9)	5.557 (7)	5.555 (3)	5.553 (8)
c (Å)	7.763 (8)	7.772 (3)	7.789 (4)	7.822 (1)	7.856 (6)
Cell volume (Å^3)	236.46 (6)	236.74 (3)	237.56 (9)	238.97 (4)	240.69 (0)
Nd/Ba (x, y, 0.25) (4c)					
x	0.987 (4)	0.987 (8)	0.993 (8)	0.994 (5)	0.996 (2)
y	0.047 (9)	0.041 (6)	0.033 (2)	0.022 (7)	0.013 (5)
Fe (0.5, 0, 0) (4b)					
O_1(x, y, 0.25) (4c)					
x	0.089 (4)	0.100 (9)	0.117 (2)	0.088 (7)	0.065 (6)
y	0.475 (5)	0.506 (2)	0.496 (3)	0.468 (9)	0.512 (6)
O_2(x, y, z) (8d)					
x	0.708 (6)	0.785 (4)	0.715 (4)	0.783 (5)	0.783 (3)
y	0.297 (4)	0.288 (7)	0.261 (7)	0.231 (2)	0.212 (6)
z	0.037 (1)	0.036 (2)	-0.016 (6)	-0.016 (6)	0.018 (7)
Bond angles (°)					
$< Nd/Ba - O - Fe >_{avg}$	59.063	92.554	93.272	93.263	93.068
$< Fe - O - Fe >_{avg}$	152.52	154.52	155.19	158.09	160.26
Bond length (Å)					
$< Nd/Ba - O >_{avg}$	2.533	2.578	2.639	2.701	2.672
$< Fe - O >_{avg}$	2.003	1.992	1.994	1.987	1.987
Tolerance factor	0.87 (2)	0.91 (4)	0.94 (0)	0.95 (1)	0.96 (1)
R_{wp}(%)	16.6	13.3	30.9	33.1	33.4
R_p(%)	9.14	8.2	22.1	23.9	23.9
χ^2	1.15	1.42	0.798	0.845	0.864

Table 2. Crystallite sizes (D_{scher} and $D_{W\text{-}H}$), lattice strain (ε), and particle size data ($< D >_{SEM}$ and σ_D) for $Nd_{1-x}Ba_xFeO_3$ samples.

Sample	NFO	x=0.1	x=0.2	x=0.3	x=0.4
D_{scher} (nm)	47±0.5	52±0.6	42±0.1	30±0.1	30±0.1
$D_{W\text{-}H}$ (nm)	61±0.7	65±0.9	47±0.7	23±0.4	22±0.1
ε	4.12×10^{-4}	9.14×10^{-4}	1.43×10^{-3}	1.44×10^{-3}	$.\backslash 63\times 10^{-3}$
$< D >_{SEM}$ (nm)	98±0.5	80±0.7	43±0.3	38±0.8	32±0.5
$\sigma_D(nm)$	15.7±0.2	22.5±0.2	3.6±0.9	5.5±0.6	3.7±0.9

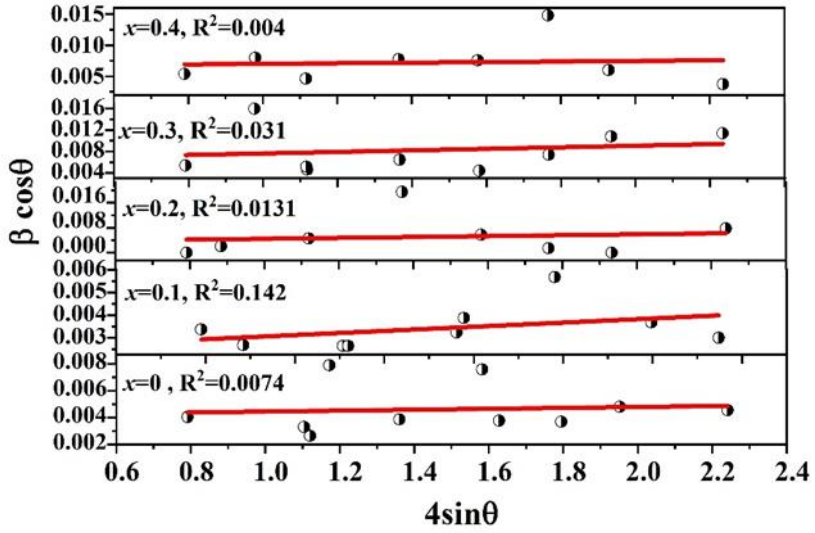

Fig. 4. The W–H plot of $Nd_{1-x}Ba_xFeO_3$.

In Eq. 3, $(Nd/Ba-O)_{avg}$ and $(Fe-O)_{avg}$ represent the average bond lengths between the respective ions and oxygen atoms. This tolerance factor serves as a reliable criterion for evaluating the stability and symmetry of the orthorhombic perovskite structure [23]. According to Figure 3(d), the τ value increases with higher Ba^{2+} substitution, indicating a trend toward higher structural symmetry. Moreover, the average Fe–O–Fe bond angle increased from approximately 152.52° in the pristine sample to about 160.26° in the sample with x = 0.4. In summary, the collective trends (including the reduction in the octahedral tilt angle Φ, increase in τ, and decrease in the orthorhombic strain) all point to a decrease in the structural distortion. Given the relatively large ionic radius of Ba^{2+}, such behavior is expected and suggests that the crystal structure is evolving toward a more symmetric (likely tetragonal) phase. To calculate the crystallite size, the Debye–Scherrer equation was initially used:

$$D_{Scher} = \frac{k\lambda}{\beta\cos\theta} \quad (4)$$

In this relation: θ is the Bragg angle, β is the full width at half maximum (FWHM) of the diffraction peak, λ= 1.542 Å is the wavelength of the X-ray radiation, D is the crystallite size, k = 0.94 is the Scherrer constant, which depends on the particle shape and structure. The calculated values for the crystallite size and lattice strain are presented in Table 2. To obtain a more accurate estimation of the crystallite size, the W–H method was also employed. This method considers the peak broadening in XRD to arise not only from the crystallite size but also from the lattice strain (ε). Following previous studies, the W–H analysis was performed by plotting $\beta\cos\theta$ versus $4\sin\theta$ (Fig. 4)[18]. By fitting a straight line to the data, the crystallite size was obtained from the intercept, and the lattice strain was determined from the slope. The results are summarized in Table 2.

3.2. Microstructural analysis

Fig. 5 presents the FE-SEM images of all samples at a magnification of 50,000. These images were used to investigate the surface morphology and to determine the average particle size. For the quantitative analysis of the particle size distribution, the image data were analyzed using Digimizer software, and the corresponding histograms were extracted after applying the log-normal fitting. This approach aligns with the methods reported in previous studies [24, 25]. Based on this analysis, the average particle size $\langle D\rangle_{SEM}$ and standard deviation (σ) for each sample were determined and reported in Table 2 [18]. The results indicate that with increasing Ba^{2+} ion substitution, the average particle size decreased from 98 nm for the base composition to approximately 32 nm for the x = 0.4 composition. This reduction is primarily attributed to the effects of lattice strain and defect formation, especially oxygen vacancies. Substitution of Ba^{2+} ions for Nd^{3+} introduces stress to the crystal structure, leading to the formation of structural defects and lattice strain. These strains and defects limit the free growth of crystals, ultimately resulting in smaller particle sizes.

Additionally, the reduction in nuclear charge due to the substitution of Ba^{2+} for Nd^{3+} may also contribute to this process. Similar behavior has been reported in the study by Gao et al. for Ba substitution up to 0.15 in $NdFeO_3$ [26], as well as in Sr substitution in $YFeO_3$ by Kumar et al [27]. Gao attributed this reduction to the creation of lattice defects, which promote grain agglomeration and adhesion, resulting in more grain boundaries [26]. To confirm the chemical composition of the synthesized powders and to examine the stoichiometric ratios of their constituent elements, the EDX analysis was performed (Fig. 6). Despite its relative simplicity, this technique serves as a powerful tool for identifying the elemental composition of materials. The peak heights in the EDX spectra correspond to the atomic or weight percentages of the ions present in the samples.

3.3. Optical band gap analysis

To investigate the effect of barium ion substitution at different concentrations on the electronic structure of $NdFeO_3$, the DRS analysis was employed. In this regard, and consistent with previous studies, the K–M function was applied in the form [9, 28, 29].

$$F(R) = (1-R)^2/2R \quad (5)$$

Where $F(R)$ is the K-M function and R is the reflectance coefficient of the samples. As shown in Figure 7(a), the plots of $[F(R)h\nu]^2$ versus $h\nu$ were obtained for the various samples, and by fitting the linear region, the E_g values were extracted. It should be noted that the electronic transition in this analysis is considered to be of the direct type. The trend of E_g as a function of Ba^{2+} concentration is presented in Figure 7(b). The results indicate that with increasing Ba content, E_g decreases from 2.15 eV in the pristine sample to 1.28 eV in the sample with x = 0.4. Generally, three fundamental parameters influence the variation of the E_g in orthoferrites: (i) the Fe–O bond length, (ii) the particle size, and (iii) the presence of oxygen vacancies. Each of these factors is discussed in detail below.

(i) Fe–O Bond Length: The Fe–O bond length serves as an indicator of the degree of orbital overlap between the O-2p and Fe-3d states in the crystal lattice. Although Ba^{2+} has a larger ionic radius compared to Nd^{3+}, Table 1 shows that with increasing Ba concentration, the average Fe–O bond length changes only slightly, from 2.003 to 1.98 Å. This variation is negligible. According to a previous report on rare-earth orthoferrites ($RFeO_3$, R = La–Yb), where the Fe–O bond length varied only in the range of 2.006–2.013 Å, the optical band gap remained nearly constant at 1.94–1.97 eV [7]. Therefore, the pronounced reduction of E_g observed in the present compositions cannot only be explained by the changes in the Fe–O bond length.

(ii) Particle Size: According to Table 2, increasing the Ba concentration leads to a decrease in the average particle size from 98 nm to 32 nm. It is well established that the E_g of semiconductor materials increases as the particle size decreases [30-32]. In contrast, in many orthoferrite systems, a reduction in the band gap has instead been correlated with an increase in the particle size [33, 34]. Consequently, the observed decrease in particle size does not provide a sufficient explanation for the substantial reduction of E_g in the present samples.

(iii) Oxygen Vacancies: In the previous study on XPS analysis of Ba-substituted $NdFeO_3$ (up to x=0.15) revealed that oxygen vacancies begin to appear at $x \geq 0.1$, with their concentration increasing systematically with further Ba incorporation [26]. This phenomenon arises from the substitution of Ba^{2+} for Nd^{3+}, which disrupts the charge neutrality. To maintain charge balance, some Fe^{3+} ions are partially oxidized to Fe^{4+}. The resulting increase in oxygen vacancies alters the electronic structure, introducing mid-gap states (sub-bands) between the valence and conduction bands, ultimately leading to a significant reduction in E_g. Similar behavior has been documented in $Bi_{1-x}Ba_xFeO_3$ [35], $La_{1-x}Ca_xFeO_3$[36], and Mg-substituted $LaFeO_3$ [15]. Notably, in some perovskite compounds, such as $LaFeO_3$ substituted with Sr or Ca at x = 0.2, the density of oxygen vacancies is so high that the band gap essentially collapses, giving rise to a semi-metallic character [15]. Accordingly, it can be concluded that the presence of oxygen vacancies plays a key and decisive role in the reduction of the band gap in the present compounds. These findings are highly significance for the rational design of advanced materials for photocatalytic, sensing, and energy storage applications, as they illustrate how ionic substitution can be systematically employed to modulate the optical properties of perovskite and orthoferrite compounds.

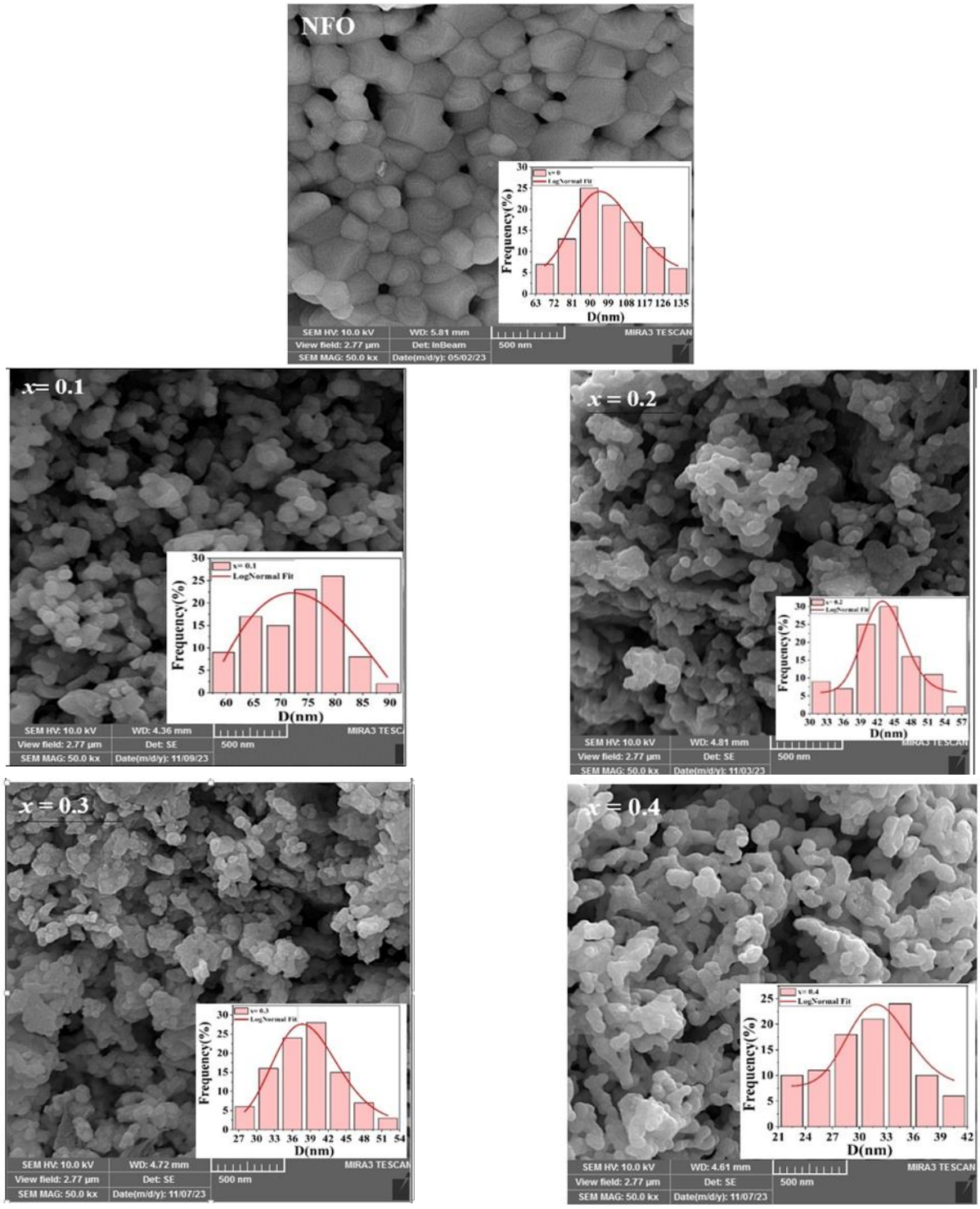

Fig. 5. The FE-SEM images for all samples.

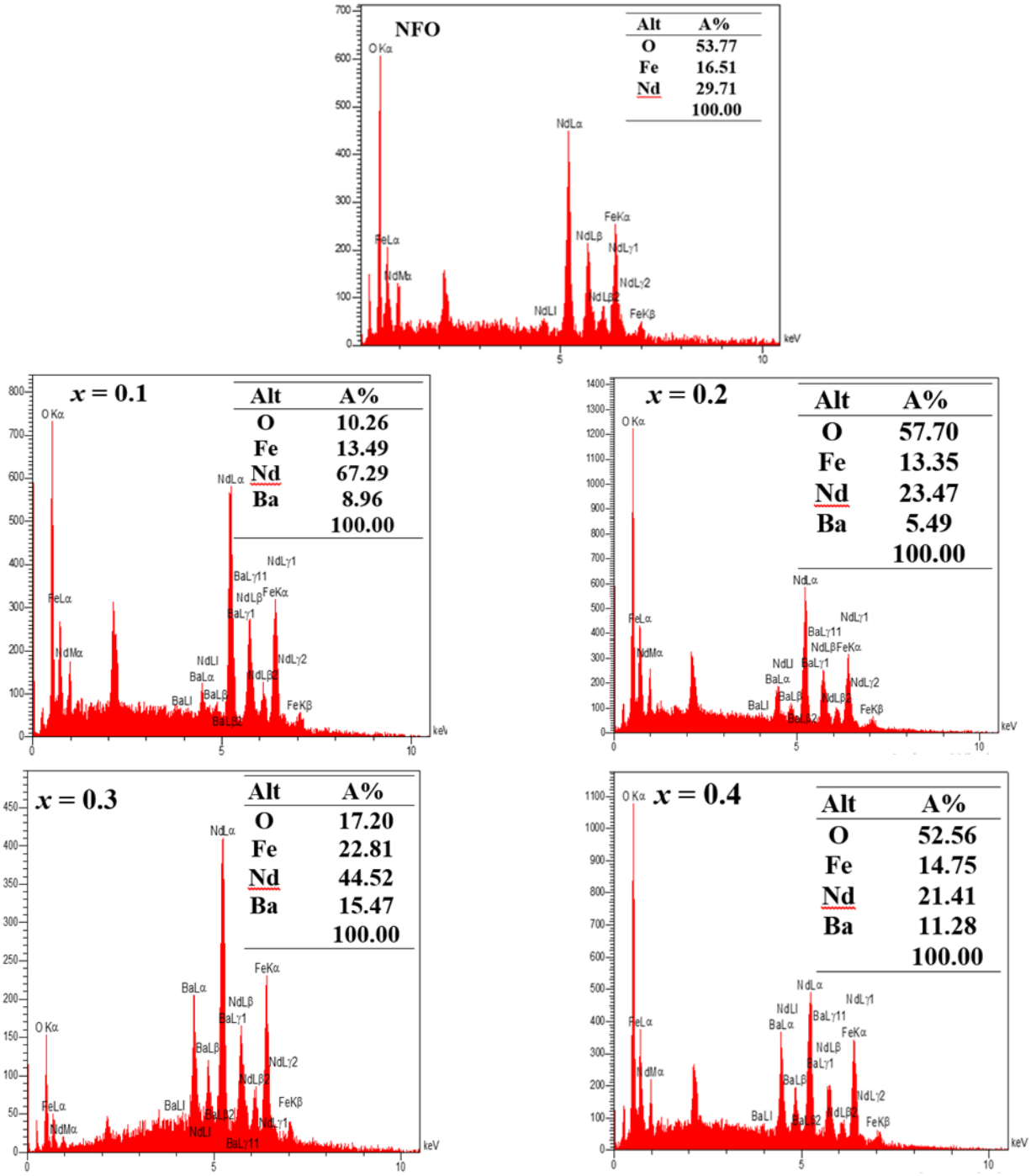

Fig. 6. EDX spectra and elemental composition (atomic %) of $Nd_{1-x}Ba_xFeO_3$.

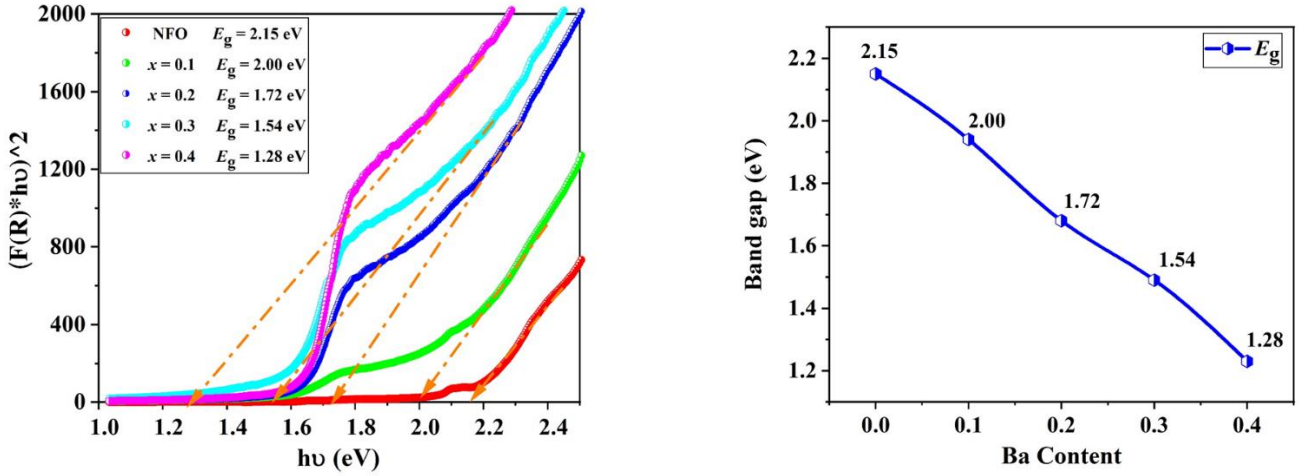

Fig. 7. (a) $(F(R)*hv)^2$ versus photon energy curve for $Nd_{1-x}Ba_xFeO_3$,**(b)** Optical band gap variation as a function of Ba concentration.

4. Conclusions

$Nd_{1-x}Ba_xFeO_3$ nanoparticles were successfully synthesized via the sol–gel method, and the effects of divalent Ba^{2+} substitution at the Nd^{3+} site were systematically investigated across different concentrations. The XRD analysis confirmed that all the samples retained approximately a single-phase orthorhombic structure. However, with increasing Ba^{2+} content, a gradual reduction in the lattice distortion, an increase in the tolerance factor, and a tendency toward higher structural symmetry were observed. The microstructural characterization revealed a notable reduction in the average particle size, which can be attributed to the suppressed grain growth induced by the lattice strain and ionic substitution. Furthermore, the DRS analysis showed a substantial narrowing of the E_g, decreasing from 2.15 eV in the parent compound to 1.28 eV in the sample with 40% Ba doping. This band gap reduction is primarily ascribed to the generation of oxygen vacancies that lead to modifications in the electronic structure. The tunable band gap and enhanced visible light absorption make these nanoparticles suitable for photo-catalytic applications, particularly in the degradation of organic pollutants. Moreover, the observed changes in surface properties and the concentration of oxygen vacancies indicate their potential for use in gas and chemical sensors. Overall, Ba^{2+} doping in $NdFeO_3$ not only improves its crystal, microstructural, and optical properties but also expands its functional applicability in photo-catalysis, sensing, optoelectronics, and photo-electrochemical devices. These findings highlight Ba-doped $NdFeO_3$ as a promising candidate for the development of advanced materials and devices across various technological fields.

Funding Statement

This research received no specific grant from any funding agency.

Conflicts of interest

The authors declare that they have no known competing financial interests or personal relationships that could have appeared to influence the work reported in this paper.

Authors contribution statement

Mansoureh Pourjafar: Data analysis and experimentation, Manuscript writing and editing, Data analysis and interpretation. **Davoud Sanavi Khoshnoud:** Conceptualization and study design, Manuscript writing and editing, Data analysis and interpretation, Supervision and project administration.

References

[1] Wu, Z.L., Zhang, R., Zhao, M., Fang, S.M., Han, Z.X., Hu, J.F. and Wang, K.Y., 2012. Effect of Pd doping on the acetone-sensing properties of $NdFeO_3$. *International Journal of Minerals, Metallurgy, and Materials*, *19*(2), pp.141-145.

[2] Li, X.B., Gao, C., Sun, S., Huang, L.L., Zhou, H., Wu, B.X., Zheng, L.H., Kang, X.F., Zhao, Y.X., Wang, F.P. and Zhang, J.B., 2024. Ethanolamine gas sensors based on $NdFeO_3$ modified hexagonal pyramid shaped ZnO nanocrystals. *Ceramics International*, *50*(15), pp.26311-26324.

[3] Guo, J., Ma, S., Ma, N., Liu, J., Wei, J., Xu, C., Fan, G. and Ni, P., 2024. Hydrothermal synthesis of $NdFeO_3$ nanoparticles and their high gas-sensitive properties. *Ceramics International*, *50*(21), pp.43654-43664.

[4] Omari, E. and Omari, M., 2022. Enhancing catalytic activity of $NdFeO_3$ perovskite by tuning A-site cation deficiency for oxygen evolution reaction. *International Journal of Hydrogen Energy*, *47*(32), pp.14542-14551.

[5] Al-Abbad, E.A., Aadil, M., Aldrdery, M., Alkhaldi, N.D., Khalid, A., Alrahili, M.R., Algarni, M., El Jery, A. and El-Aassar, M.R., 2024. Nanostructured codoped neodymium orthoferrite synthesized via the hydrothermal route for photocatalytic annihilation of crystal violet dye. *Ceramics International*, *50*(24), pp.54943-54954.

[6] Ukorah, I.N., Owolabi, A.J., Ali, H., Onimisi, M.Y., Tafida, R.A., Olalekan, A.J., Gambo, H.M., Usman, S.L., Christiana, A.O., Ukwenya, J.M. and Akinade, B.J., 2024. Investigating the Performance of TIN-Based Perovskite Solar Cell with Zinc Selenide as an ETM and Graphene as an HTM Using SCAPS-1D. *Progress in Physics of Applied Materials*, *4*(2), pp.171-181.

[7] Warshi, M.K., Mishra, V., Sagdeo, A., Mishra, V., Kumar, R. and Sagdeo, P.R., 2018. Structural, optical and electronic properties of $RFeO_3$. *Ceramics International*, *44*(7), pp.8344-8349.

[8] Rajabi, Y., Gholizadeh, A. and Gorzoddin, M., 2025. Investigating the Nonlinear Optical Behavior of $La_{1-x}Ca_xCo_{0.5}Mg_{0.5}O_3$ Perovskites. *Progress in Physics of Applied Materials*, *5*(1), pp.47-62.

[9] Nakhaei, M., Khoshnoud, D.S., Bremholm, M., Nobre, M.A. and Khonakdar, H.A., 2023. Effects of Al doping on physical properties and photocatalytic activity of neodymium orthoferrite. *Journal of Sol-Gel Science and Technology*, *105*(1), pp.246-265.

[10] Kotnana, G. and Hong, S., 2025. Recent Progress on Rare Earth Orthoferrites for Gas-Sensing Applications. *Chemosensors*, *14*(5).

[11] Bez, R., Maayoufi, A.E., Bouhmouche, A., Moubah, R. and Mliki, N.T., 2024. Structural, dielectric, optical and electronic properties of $NdFeO_3$: experimental and computational study. *Journal of Materials Science: Materials in Electronics*, *35*(20), p.1403.

[12] Qamar, F., Sharma, S. and Khan, S., 2024. Effect of Ce^{3+} ion substitution on the structural, optical, electrical and ferroelectric properties of $NdFeO_3$ nanoparticles. *Applied Physics A*, *130*(9), p.626.

[13] Li, X.B., Zhou, H., Huang, L.L., Gao, C., Zhang, Q.Q., Wu, B.X., Sun, S. and Wang, A.Q., 2025. Detection of formaldehyde sensitive properties of Sm^{3+} doped $NdFeO_3$. *Journal of Alloys and Compounds*, *1010*, p.176933.

[14] Kashyap, S.J., Sankannavar, R. and Madhu, G.M., 2022. Insights on the various structural, optical and dielectric characteristics of $La_{1-x}ca_xFeO_3$ perovskite-type oxides synthesized through solution-combustion technique. *Applied Physics A*, *128*(6), p.518.

[15] Nandy, S., Theingi, M., Ghosh, S., Chae, K.H. and Sudakar, C., 2024. Influence of local structure and metal-oxygen hybridization on the electrical and magnetic properties of alkaline earth metal (Mg^{2+}, Ca^{2+}, Sr^{2+}) substituted $LaFeO_3$ ceramics. *Journal of Applied Physics*, *136*(10).

[16] Wang, M., Cheng, L., Huang, L., Pan, S., Yao, Q., Hu, C., Liang, Q. and Zhou, H., 2021. Effect of Sr doped the $YFeO_3$ rare earth ortho-ferrite on structure, magnetic properties, and microwave absorption performance. *Ceramics International*, *47*(24), pp.34159-34169.

[17] Ali, S.A., Naseem, S., Khan, W. and Nambissan, P.M.G., 2019, December. Alkaline earth cation substitution effects in $LaFeO_3$ OrthoFerrite nanocrystals studied by positron annihilation. In *AIP Conference Proceedings* (Vol. 2182, No. 1, p. 050028). AIP Publishing LLC.

[18] Nakhaei, M. and Khoshnoud, D.S., 2019. Influence of particle size and lattice distortion on magnetic and dielectric properties of $NdFeO_3$ orthoferrite. *Physica B: Condensed Matter*, *553*, pp.53-58.

[19] Berezhnaya, M.V., Perov, N.S., Almjasheva, O.V., Mittova, V.O., Nguyen, A.T., Mittova, I.Y., Druzhinina, L.V. and Alekhina, Y.A., 2019. Synthesis and magnetic properties of barium-doped nanocrystal lanthanum orthoferrite. *Russian Journal of General Chemistry*, *89*(3), pp.480-485.

[20] Makhdoom, A.R., Shah, S.M., Mahmood, T., Iqbal, M.J., Akhtar, M.J. and Rafiq, M.A., 2019. Enhancement of ferromagnetism by suppression of spiral spin structure in Ba doped $BiFeO_3$. *Journal of Magnetism and Magnetic Materials*, *484*, pp.286-290.

[21] Hait, S., Ghose, S. and Mandal, K., 2020. Effect of Ba and Y co-doping on the structural and magneto-electric properties of $BiFeO_3$ ceramic. *Journal of Alloys and Compounds*, *822*, p.153614.

[22] Dehno, R.T. and Khoshnoud, D.S., 2022. Multiferroic properties in $Sm_{1-x}Er_xFeO_3$ ceramics. *Journal of Magnetism and Magnetic Materials*, *541*, p.168515.

[23] Pourjafar, M. and Khoshnoud, D.S., 2025. A comparative study on effects of magnesium substitution at Nd and Fe-sites on the structural, optical, magnetic, and dielectric properties of neodymium orthoferrite. *Results in Physics*, p.108496.

[24] Ghasemi, E. and Khoshnoud, D.S., 2025. The effect of Mg doping on spin reorientation transition and physical properties of $SmFeO_3$. *Journal of Materials Science: Materials in Electronics*, *36*(5), p.304.

[25] Nakhaei, M., Nobre, M.A., Khoshnoud, D.S., Bremholm, M. and Khonakdar, H.A., 2025. Chemical synthesis, structural and magnetic properties of Al-doped neodymium orthoferrite. *Journal of Alloys and Compounds*, *1010*, p.176987.

[26] Gao, X., Ji, Y., Wang, M. and Liang, Q., 2024. Effect of Ba substitution on structure, magnetic properties and microwave properties of $NdFeO_3$. *Materials Today Communications*, *38*, p.108264.

[27] Kumar, D., Yadav, S., Singh, C.B., Yadav, R.S., Rai, S.B. and Singh, A.K., 2023. Impact of Sr^{2+} doping on the structural, dielectric, ferroelectric and optical properties of $YFeO_3$ perovskite phosphor. *Journal of Alloys and Compounds*, *945*, p.169286.

[28] Muneeswaran, M., Jang, J.W., Jeong, J.H., Akbari-Fakhrabadi, A. and Giridharan, N.V., 2019. Effect of dopant-induced defects on structural, electrical, and enhanced ferromagnetism and magnetoelectric properties of Dy and Sr co-doped $BiFeO_3$. *Journal of Materials Science: Materials in Electronics*, *30*(8), pp.7359-7366.

[29] Arabi, A., Fazli, M. and Ehsani, M.H., 2022. Photocatalytic activity of the $La_{0.7}Ca_{0.3}MnO_3$ nanorods. *Progress in Physics of Applied Materials*, *2*(2), pp.123-131.

[30] Abdullah, B.J., 2022. Size effect of band gap in semiconductor nanocrystals and nanostructures from density functional theory within HSE06. *Materials Science in Semiconductor Processing*, *137*, p.106214.

[31] Singh, M., Goyal, M. and Devlal, K., 2018. Size and shape effects on the band gap of semiconductor compound nanomaterials. *Journal of Taibah University for Science*, *12*(4), pp.470-475.

[32] Mishra, S., Pandey, B.K., Jaiswal, R.L. and Gupta, J., 2024. Unified model for the studies of band gap of nanosolids with their varying shape and size. *Chemical Physics Letters*, *841*, p.141177.

[33] Duyen, P.T.H., Diem, C.H. and Tien, N.A., 2022. Cd-doped $NdFeO_3$ nanoparticles: synthesis and optical properties study. *Journal of Materials Science: Materials in Electronics*, *33*(7), pp.3546-3555.

[34] Chung, N.T.K., Tien, N.A., Diem, C.H. and Vuong, B.X., 2022. Structural and optical properties of Sr-doped $NdFeO_3$ nanoparticles prepared by a simple co-precipitation method. *Journal of Chemical Sciences*, *134*(1), p.34.

[35] Liang, N., Wang, C., Yao, X., Wang, X., Yan, T., Wang, R., Jin, Q., Guo, X., Guo, E., Ge, C. and He, M., 2024. Structure evolution and energy band modulation in Ba-doped $BiFeO_3$ thin films. *Journal of Applied Physics*, *135*(4).

[36] Srinatha, N., Reddy, S.S., Al-Dossari, M., Gurushantha, K., Abd EL-Gawaad, N.S., Manjunatha, S.O., Kumar, K.R., Kumar, M.S., Tangod, V.B. and Madhu, A., 2024. Effect of aliovalent substitution in the band structure engineered Ca^{2+}-doped $LaFeO_3$ nanoparticles for visible light-induced photocatalytic studies. *Ceramics International*, *50*(1), pp.1836-1848.